Quantum oscillations in kagome metals $CsTi_3Bi_5$ and $RbTi_3Bi_5$

Zackary Rehfuss [1] Christopher Broyles,[1] David Graf,[2] Yongkang Li,[3] Hengxin Tan,[3] Zhen Zhao,[4,5] Jiali Liu,[4,5] Yuhang Zhang,[4,5] Xiaoli Dong,[4,5] Haitao Yang,[4,5] Hongjun Gao,[4,5] Binghai Yan [3] and Sheng Ran[1]

[1]*Department of Physics, Washington University in St. Louis, St. Louis, Missouri 63130, USA*
[2]*National High Magnetic Field Laboratory, Florida State University, Tallahassee, Florida 32310, USA*
[3]*Department of Condensed Matter Physics, Weizmann Institute of Science, Rehovot 7610001, Israel*
[4]*Beijing National Center for Condensed Matter Physics and Institute of Physics, Chinese Academy of Sciences, Beijing 100190, PR China*
[5]*School of Physical Sciences, University of Chinese Academy of Sciences, Beijing 100190, PR China*

We report quantum oscillation measurements on the kagome compounds ATi_3Bi_5 (A=Rb, Cs) in magnetic fields up to 41.5 T and temperatures down to 350 mK. In addition to the frequencies observed in previous studies, we have observed multiple unreported frequencies above 2000 T in $CsTi_3Bi_5$ using a tunnel diode oscillator technique. We compare these results against density functional theory calculations and find good agreement with the calculations in the number of peaks observed, frequency, and the dimensionality of the Fermi surface. For $RbTi_3Bi_5$ we have obtained a different quantum oscillation spectrum, although calculated quantum oscillation frequencies for the Rb compound are remarkably similar to the Cs compound, calling for further studies.

I. INTRODUCTION

The Kagome lattice is a rich playground for investigating fundamental physics and uncovering new, exotic phases of matter. Not only does this lattice display features such as flat bands, Van Hove singularities, Dirac points, Dirac cones, highly anisotropic Fermi surfaces, and Fermi surface nesting, but it also hosts a plethora of exotic phases, including frustrated magnetism, quantum spin liquids, chiral spin states, and various topological phases.

Previous studies on kagome lattice materials include the observation of Weyl fermions in the ferromagnet $Co_3Sn_2S_2$ [1,2], magnetic skyrmions in the noncollinear antiferromagnet Fe_3Sn_2 [3–5], flat bands and Dirac points in antiferromagnetic FeSn [6], and paramagnetic CoSn [7,8], chiral spin textures in the noncollinear antiferromagnet Mn_3X (X=Sn, Ge) [9,10], and the observation of large anomalous hall effects in many of these kagome systems [11]. More recently, new families of kagome lattice materials have been discovered such as the which have a large chemical tunability and shows an array of magnetic phases [12,13]. Another family, Nb_3X_8 (X = Cl, Br, I), have a trigonally distorted breathing mode kagome lattice which have prominent isolated flat bands and are proposed to be possible Mott insulators or obstructed atomic insulators [14].

Another family that has attracted significant interest is the AV_3Sb_5 (A=K, Cs, Rb) system (the "135" compounds). This family has been a hot topic in recent years due to the observation of multiple competing phases such as superconductivity, charge and pair density waves, nematic ordering, and a large anomalous hall effect in a single material [15–35]. A recent discovery has found that replacing vanadium with chromium leads to a new compound, $CsCr_3Sb_5$, that exhibits multiple phases and becomes superconducting under applied pressure [36,37]. These complex symmetry breaking ordered states are found to compete or intertwine with each other, much like the situation of the high temperature superconductors [38].

The recently discovered ATi_3Bi_5 (A=Rb,Cs) compounds represent another family that is isostructural to the AV_3Sb_5 compound, but differ vastly in their emergent phenomena. Magnetic and electrical measurements have not revealed any magnetic or charge order down to the superconducting transition near 4.8 K [39,40]. Therefore this system becomes a perfect candidate to study the intrinsic electronic structure of the kagome lattice that is not intermingled with any type of magnetic or charge ordering. First principles calculations and photo-emission measurements have identified essential features of the band structure due to the kagome lattice, including flat band, Dirac nodal loops, and nodal lines [41–43]. Another way to measure the Fermi surface is to measure quantum oscillation frequencies. Quantum oscillation frequencies have been calculated for ATi_3Bi_5, which demonstrate a strong 3D signature despite their cylinderlike Fermi surface geometry [44]. The Quantum oscillation measurements have previously been carried out in low magnetic field, which only revealed relatively low frequencies [44–46]. In this work we report quantum oscillation measurements on both $CsTi_3Bi_5$ and $RbTi_3Bi_5$, in magnetic field up to 41.5 T. For the Cs compound, our results reveal four frequencies above 2000 T, consistent with DFT calculations. The Rb compound has different frequency spectrum from that of the Cs compound, which is likely due to a different Fermi energy.

II. METHODS

The samples were grown using a self-flux method outlined elsewhere [39]. Due to the air sensitive nature of the ATi_3Bi_5 compounds, special handling was taken to minimize oxidization. To store the samples long term, they were stored in liquid nitrogen inside a Dewar. While transporting the samples, they
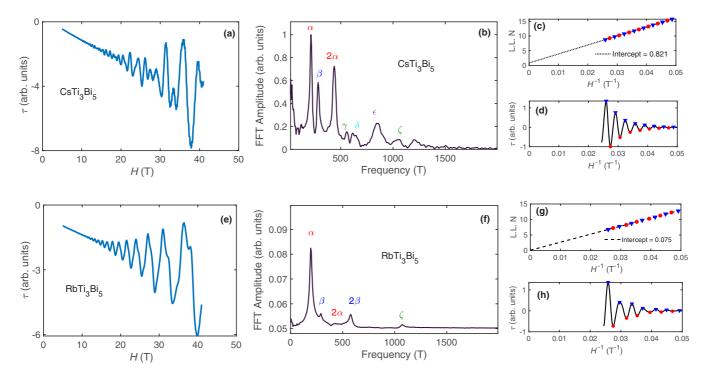
FIG. 1. (a), (e) Magnetic torque vs magnetic field (H) for CsTi$_3$Bi$_5$ and RbTi$_3$Bi$_5$, respectively. (b), (f) Fourier transform amplitude vs frequency at $\theta = 0$ degrees for CsTi$_3$Bi$_5$ and RbTi$_3$Bi$_5$, respectively, with labels showing fundamental frequencies and harmonics. (c), (g) Landau fan diagram showing Landau Level N vs inverse field for the α frequency peak for CsTi$_3$Bi$_5$ (c) and RbTi$_3$Bi$_5$ (g). Magnetic torque vs inverse field (1/H) with a band-pass filter set between 200 T and 250 T to isolate out the α frequency contribution to construct the Landau fan diagram for for CsTi$_3$Bi$_5$ (d) and RbTi$_3$Bi$_5$ (h).

were sealed in quart ampules that were filled with argon gas at 0.33 bar. Before the experiments, the samples were exposed to air briefly for mounting them onto the experiment platforms. The samples were optically inspected and samples were selected with nominal thickness under 100 μm and a surface area of roughly 200 μm×200 μm, then they were encapsulated in GE varnish on the experimental platforms. Quantum oscillation measurements were performed at the high magnetic field laboratory in Tallahassee, Florida using a tunnel diode oscillator (TDO) technique [47,48] and a piezoresistive torque cantilever technique in fields up to 41.5 T and temperatures down to 350 mK. The torque and TDO signal were background subtracted using a combination of Gaussian filtering and a third order polynomial fit. All the analysis of quantum oscillation data was carried out using Matlab 2023a with the curve fitter and signal analyzer toolboxes.

For the density functional theory (DFT) calculations, crystal structures of CsTi$_3$Bi$_5$ and RbTi$_3$Bi$_5$ are fully relaxed with the Vienna *ab initio* simulation package (VASP) [49], where the Perdew-Burke-Ernzerhof [50] type generalized gradient approximation is employed to mimic the electron-electron interaction. The cutoff energy for the plane-wave basis set is 300 eV, and a k mesh of $12\times12\times6$ is used to sample the Brillouin zone. The DFT-D3 vdW correction [51] is considered in the structural relaxation. After that, the full potential local orbital (FPLO) software [52] is used to fit the band structure for the tight-binding Hamiltonians of both materials with the wannier basis set composed of Ti d and Bi p orbitals. The spin-orbital coupling and a k mesh of $12\times12\times6$ are employed. Fermi surfaces of CsTi$_3$Bi$_5$ and

RbTi$_3$Bi$_5$ are calculated from the tight-binding Hamiltonians. The detailed method for quantum oscillation frequency and phase calculation based on the Fermi surface can be found in Refs. [44,53].

III. RESULTS

To study the Fermi surface in the ATi$_3$Bi$_5$ (A=Cs,Rb) family, we measured magnetic torque (τ) and TDO frequency as a function of magnetic field strength, angle, and temperature. Figures 1(a) and 1(e) show the torque signal measured as a function of magnetic field at 350 mK for CsTi$_3$Bi$_5$ and RbTi$_3$Bi$_5$, respectively. Clear quantum oscillations can be seen across the entire field range for both compounds, with the Cs compound showing more apparent frequency components than the Rb compound in the raw data. Figures 1(b) and 1(f) show the discrete Fourier transform (FFT) of the background subtracted torque signal vs inverse field for the Cs and Rb compounds for the applied field perpendicular to the kagome plane ($\theta = 0$).

We observe multiple frequency peaks for frequencies below 1500 T in both compounds. Some frequency peaks might be harmonics. To identify harmonic peaks, we check the ratio with fundamental frequencies across all observable angles and see if this ratio remained constant and an integer (Fig. S3 of Supplemental Material [56]). For the Cs one, there are multiple peaks with similar frequencies, making it difficult to distinguish between fundamental peaks and harmonics for some frequencies. With the assistance of DFT calculations (discussed later), we identified six fundamental frequency
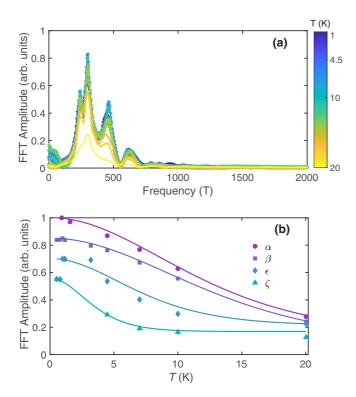
FIG. 2. (a) Temperature dependence of the Fourier transform amplitude vs frequency, at $\theta = 40$ degrees, of the background subtracted torque signal vs $1/H$ for CsTi$_3$Bi$_5$. (b) Lifshitz-Kosevich fitting for the temperature dependence of the Fourier transform amplitudes for the observed fundamental frequency peaks.

FIG. 3. (a) Angular dependence of the Fourier transform amplitude (offset for clarity) vs frequency of the background subtracted torque signal vs $1/H$ for the CsTi$_3$Bi$_5$ torque measurement. (b) $1/\cos(\theta)$ fitting for the angular dependence of the Fourier transform frequency in the for the observed fundamental frequency peaks.

peaks at 216 T (α), 284 T (β), 557 T (γ), 630 T (δ), 850 T (ϵ), and 1060 T (ζ), and a suspected harmonic peak at 438 T (2α). The frequency spectra for Rb torque measurements appear to be different from that for the Cs one, even excluding harmonic peaks. In the Rb Sample we observed three fundamental frequency peaks at 193 T (α), 290 T (β), and 1070 T (ζ), and two suspected harmonic peaks at 430 T (2α) and 580 T (2β). In the high frequency range, we observed a frequency peak around 4500 T for Rb shown in Fig. S4 of Supplemental Material [56]. This frequency peak was only clearly observed at one angle (θ=32 degrees), and was very broad. Due to the broadness of the peak and it only being observed at one angle, this peak may not correspond to real quantum oscillations.

Figures 1(c) and 1(g) show the Landau fan diagram made for the lowest frequency peak for the Cs and Rb compound, respectively. The lowest frequency peak was isolated in the raw data using a band-pass filter and the signal is plotted vs inverse field [Figs. 1(d) and 1(h)]. The maxima were assigned to n+3/4 and and minima were assigned to n+1/4. Then the intercept was calculated by extrapolating the linear maxima and minima to zero in inverse field. We obtain an intercept of 0.821 for the Cs compound and 0.075 for the Rb compound.

In order to gain insight into the effective mass of the charge carriers in this system, we measured the temperature dependence of quantum oscillation data. The FFT for the Cs compound is shown in Fig. 2(a) at various temperatures from 350 mK to 20 K. We see a clear monotonic decrease in the amplitude of the FFT indicating that all the
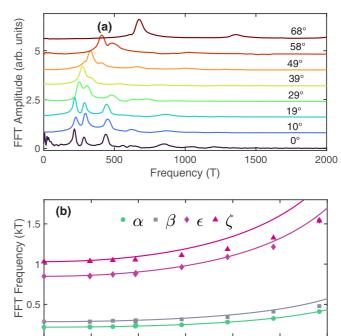
frequency peaks originate from real quantum oscillations. The temperature dependence of the normalized FFT amplitude is shown in Fig. 2(b) for a few selected fundamental frequencies. The effective masses were calculated by fitting the temperature dependence of the FFT amplitudes using the standard Lifshitz-Kosevich formalism [54,55] following Eq. (1):

$$\mathcal{A}(T) \propto \frac{\frac{\alpha m^* T}{\mu_0 H}}{\sinh\left(\frac{\alpha m^* T}{\mu_0 H}\right)}, \qquad (1)$$

where m^* is the effective mass, T is the temperature, $H^{-1} = \frac{H_{min}^{-1} + H_{max}^{-1}}{2}$ ($\mu_0 H$=8.9 T) is the average inverse magnetic field for the analysis field range, and α is defined as 14.69 T/K. The calculated effective masses, in the unit of electron mass, are 0.115 (α), 0.107 (β), 0.188 (ϵ), and 0.396 (ζ). In this analysis, we did not include the frequencies that are close to harmonic peaks.

To study the geometry of the Fermi surface, the angular dependence of the torque signal of the Cs compound was measured and is shown in Fig. 3(a) for various angles between 0 and 70 degrees. All the peak frequencies monotonically increase with the angle between the magnetic field and the c axis. At angles above 40 degrees, we see most of the peaks have begun to or already have vanished in amplitude, which is a good indicator of a 2D Fermi surface. We fit the peak frequency as a function of angle to $1/\cos(\theta)$, shown in Fig. 3(b). We see good agreement with the $1/\cos(\theta)$ fit at angles less than 30 degrees, but see a deviation from the $1/\cos(\theta)$ fit for higher angles, indicating the Fermi surface is not exactly two
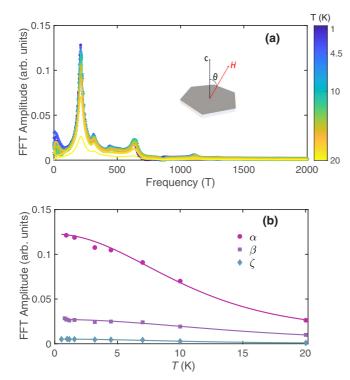
FIG. 4. (a) Temperature dependence of the Fourier transform amplitude vs frequency, at $\theta = 40$ degrees, of the background subtracted torque signal vs $1/H$ for RbTi$_3$Bi$_5$. The inset shows how we measure the angle relative to the *ab* plane. (b) Lifshitz-Kosevich fitting for the temperature dependence of the Fourier transform amplitudes for the observed fundamental frequency peaks in RbTi$_3$Bi$_5$.
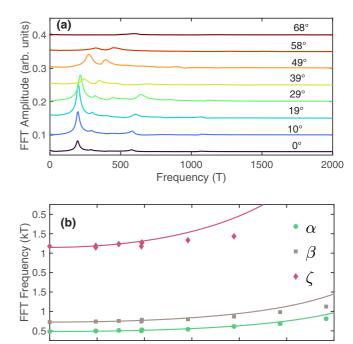

FIG. 5. (a) Angular dependence of the Fourier transform amplitude (offset for clarity) vs frequency of the background subtracted torque signal vs $1/H$ for RbTi$_3$Bi$_5$. (b) $1/\cos(\theta)$ fitting for the angular dependence of the Fourier transform frequency for the observed fundamental frequency peaks in RbTi$_3$Bi$_5$.

dimensional. Figure 4(a) shows the temperature dependence of the FFT for the torque signal of Rb compound for $\theta = 40°$. The effective masses for the fundamental frequency peaks are 0.133 (α), 0.098 (β), and 0.130 (ζ). The first two peaks α and β being similar to the Cs compound, and the third peak ζ differing significantly. Similar results were obtained for the Rb compound, as shown in Fig. 5.

Most of the frequencies observed in our torque data have been reported in the previous studies [44–46]. In order to get higher frequencies that were not previously observed, we also used a tunnel diode oscillator (TDO) technique to study the quantum oscillations, which is more sensitive to the electric conductivity than magnetic susceptibility. We observed clear but small amplitude quantum oscillations in the raw TDO signal shown in Fig. S5 of Supplemental Material [56]. The data was analyzed in two ranges: a full field range from 5 to 41 T and a high field range from 20 to 30 T up to 41 T. The full field range was used to study the low frequency (less than 2000 T) oscillations, and the high field range was used to study the high frequency oscillations ($f > 2000$ T). One of the striking differences between the torque and the TDO techniques is the number of high frequency peaks observed in the TDO data. We were able to observe the same six fundamental peaks the torque revealed in the low frequency range, and an additional four fundamental frequency peaks above 2000 T, with clear temperature dependence, shown in Fig. S10 of Supplemental Material [56] ($\theta = 40°$). The effective masses for all ten fundamental frequencies observed at $\theta = 40°$ in TDO data

are displayed in Table I with all seeming to be similar to those obtained from torque data. Angular dependence shows that these high frequency peaks also corresponds to quasi 2D Fermi surface pockets, shown in Fig. 6(g).

IV. DISCUSSIONS

Having established the Fermi surface from experiments, we now explore its origin from the DFT calculations. Band

TABLE I. Calculated and measured values of the extremal orbits of the fermi surface of CsTi$_3$Bi$_5$ at $\theta = 0°$. Column 1 is the calculated frequencies from DFT. Columns 2 and 3 are the measured frequencies from the torque and TDO measurements, respectively. Column 4 is the calculated effective mass ratio $\frac{m}{m_e}$. Columns 5 and 6 are the measured effective masses for the torque and TDO measurements, respectively.

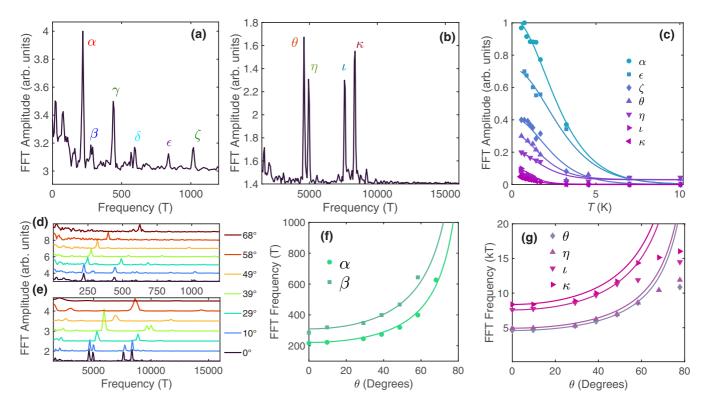|	F_{theory}(T)	F_{τ}(T)	F_{TDO}(T)	m_{theory}	m_{τ}	m_{TDO}
α	213	216	219	−0.24	0.115	0.471
β	336	284	277	−0.22	0.107	0.522
γ	542	557	438	0.22		0.305
δ	713	643	593	0.26		0.440
ϵ	802	848	838	0.24	0.188	0.545
ζ	889	1041	1019	0.32	0.396	0.474
η	4569		4601	0.72		0.720
θ	4907		4937	0.78		0.735
ι	7488		7575	1.62		1.218
κ	8111		8360	1.68		1.141

FIG. 6. (a), (b) The Fourier transform amplitude vs frequency, at $\theta = 0°$, of the background subtracted TDO signal vs $1/H$ for $CsTi_3Bi_5$ in the low and high frequency range, respectively, with peak labels. (c) Lifshitz-Kosevich fitting for the temperature dependence of the Fourier transform amplitudes for the observed fundamental frequency peaks for the $CsTi_3Bi_5$ TDO measurement. (d), (e) Angular dependence of the Fourier transform amplitude (offset for clarity) vs frequency of the background subtracted torque signal vs $1/H$ for the $CsTi_3Bi_5$ TDO measurement in the low and high frequency range, respectively. (f), (h) and (g) $1/\cos(\theta)$ fitting for the angular dependence of the Fourier transform frequency for the observed fundamental frequency peaks for the $CsTi_3Bi_5$ TDO measurement in the low and high frequency range, respectively.

structures of both materials including spin-orbital coupling (SOC) are shown in Figs. 7(a) and 7(b). Characteristic kagome band features are seen, including van Hove singularities at the M/L points (e.g., at 0.2 eV), flat bands along the M-K/L-H lines near −0.5 eV, and Dirac points at the K/H points (e.g., at about 0.5 eV) that get gapped out by SOC. Notice that there are also plenty of Dirac points along other high symmetry k paths, among which those on the Γ-M and A-L lines are type II Dirac crossings. These Dirac crossings form Dirac nodal lines in the high-symmetry planes due to the symmetry constraint [53]. These calculations are in excellent agreement with recent angle-resolved photoemission spectroscopy (ARPES) measurements [41]. There are four bands that cross the Fermi level, giving rise to five pieces of Fermi surface. Figures 7(c) and 7(d) show the calculated Fermi surfaces for $CsTi_3Bi_5$ and $RbTi_3Bi_5$, respectively. Notice that only the green Fermi surface around the M-L line is a hole pocket while all others are electron pockets.

For the Cs compound, the calculation predicts 10 frequencies to be observed at $\theta=0$ degrees shown in column 1 of Table I (see details in [44]). We break these up into two ranges for our analysis; six "low frequencies" ($f < 2000$) and 4 "high frequencies" ($f > 2000$). Our TDO data revealed six low frequencies and four high frequencies [see Fig. 6(c) and column 3 Table I], which sounds in good agreement with the calculations. In our torque data in Fig. 1(b), there are seven
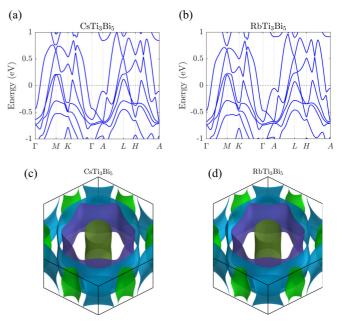

FIG. 7. (a) and (b) are the band structures of $CsTi_3Bi_5$ and $RbTi_3Bi_5$, respectively, with spin-orbital coupling. (c) and (d) are the respective Fermi surfaces. Both the band structure and Fermi surface of $RbTi_3Bi_5$ are very similar to those of $CsTi_3Bi_5$. Notice that only the green Fermi surfaces around the M-L lines are hole pockets while others are electron pockets.
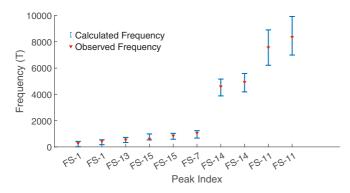
FIG. 8. Calculated and observed Fourier transform peak frequencies for $CsTi_3Bi_5$ are shown with the Fourier peak index from the DFT calculations on the x axis. The frequency dispersion per peak was calculated by tuning the Fermi level from -100 meV to 100 meV, with the error bars being the ± 100 meV values of the Fermi level.

observed low-frequency peaks, including fundamental peaks and harmonics. After excluding the harmonics following the procedure in the Supplemental Material [56], we are able to identify all six low frequencies, shown in column 2 of Table 1. We point out that the calculated frequencies show some notable differences from our observations, which might be related to the Fermi energy difference. To further verify this scenario, we calculated the quantum oscillation frequencies as a function of the Fermi energy (Fig. S11 of Supplemental Material [56]). Figure 8 shows the comparison between calculated frequencies at different Fermi energies and our measured ones. The measured frequencies fall within reasonable error bars from calculations at varied Fermi energies.

Because of the similarity in both crystal and electronic structures of $RbTi_3Bi_5$ and $CsTi_3Bi_5$, in theory, the calculated quantum oscillation frequencies for the Rb compound are remarkably similar to the Cs compound. However, we have observed a lot fewer frequencies in the Rb compound than in the Cs compound. Given the clear quantum oscillation signal of the Rb compound, this difference is unlikely related to the sample quality. One possibility is that the Fermi surface of the Rb compound might be very different from that of the calculation due to, such as doping, which can lead to different quantum oscillations. More studies are needed to elucidate the origin of the difference between Cs and Rb compounds.

Figures 1(c) and 1(g) show the Landau fan diagrams for the lowest frequency peak for the Cs and Rb compounds, respectively. The intercept of these plots is normally related to the topology of the Fermi surface. We have obtained an intercept of 0.821 for the Cs compound and 0.075 for the Rb compound, which seems to indicate a different topology of the Cs and Rb compounds and also aligns with the different oscillation spectra of these two materials. As suggested by recent theoretical studies [44,53], the quantum phase shift in materials with both inversion and time-reversal symmetries can only be one or zero. Thus, we speculate that the Fermi pocket with the lowest frequency in the Cs compound (both inversion and time-reversal symmetric) has a nontrivial quantum phase shift (0.821π is close to π) while that of the Rb compound has no phase shift (0.075π can be regarded as zero). However, we could not rule out other possible reasons, such as sample variation. More importantly, as suggested by the studies [44,53], we could not simply infer or exclude the existence of a nontrivial Berry phase in these Fermi pockets from the measured intercepts, because the quantum oscillation phase is composed of many different phases and the quantum phase shift is not a simple manifestation of the Berry phase.

To summarize, we report quantum oscillation measurements on the kagome lattice materials ATi_3Bi_5 (A=Cs,Rb) using tunnel diode oscillator and piezoelectric torque cantilever techniques for fields up to 41 T. For the Cs compound, we have observed all ten frequencies predicted by the DFT calculations, validating the Fermi surface of this family of kagome compound. The Rb compound has a different quantum oscillation spectrum, requiring further studies.

[1] Q. Wang, Y. Xu, R. Lou, Z. Liu, M. Li, Y. Huang, D. Shen, H. Weng, S. Wang, and H. Lei, Large intrinsic anomalous Hall effect in half-metallic ferromagnet $Co_3Sn_2S_2$ with magnetic Weyl fermions, Nat. Commun. **9**, 3681 (2018).

[2] E. Liu, Y. Sun, N. Kumar, L. Muechler, A. Sun, L. Jiao, S.-Y. Yang, D. Liu, A. Liang, Q. Xu, J. Kroder, V. Süß, H. Borrmann, C. Shekhar, Z. Wang, C. Xi, W. Wang, W. Schnelle, S. Wirth, Y. Chen, S. T. B. Goennenwein, and C. Felser, Giant anomalous Hall effect in a ferromagnetic kagome-lattice semimetal, Nat. Phys. **14**, 1125 (2018).

[3] L. A. Fenner, A. A. Dee, and A. S. Wills, Non-collinearity and spin frustration in the itinerant kagome ferromagnet Fe_3Sn_2, J. Phys.: Condens. Matter **21**, 452202 (2009).

[4] Z. Hou, W. Ren, B. Ding, G. Xu, Y. Wang, B. Yang, Q. Zhang, Y. Zhang, E. Liu, F. Xu, W. Wang, G. Wu, X. Zhang, B. Shen, and Z. Zhang, Observation of various and spontaneous magnetic skyrmionic bubbles at room temperature in a frustrated kagome magnet with uniaxial magnetic anisotropy, Adv. Mater. **29**, 1701144 (2017).

[5] Q. Wang, Q. Yin, and H. Lei, Giant topological Hall effect of ferromagnetic kagome metal Fe_3Sn_2, Chin. Phys. B **29**, 017101 (2018).

[6] M. Kang, L. Ye, S. Fang, J.-S. You, A. Levitan, M. Han, J. I. Facio, C. Jozwiak, A. Bostwick, E. Rotenberg, M. K. Chan, R. D. McDonald, D. Graf, K. Kaznatcheev, E. Vescovo, D. C. Bell, E. Kaxiras, J. van den Brink, M. Richter, M. Prasad Ghimire, J. G. Checkelsky, and R. Comin, Dirac fermions and flat bands in the ideal kagome metal FeSn, Nat. Mater. **19**, 163 (2020).

[7] Z. Liu, M. Li, Q. Wang, G. Wang, C. Wen, K. Jiang, X. Lu, S. Yan, Y. Huang, D. Shen, J.-X. Yin, Z. Wang, Z. Yin, H. Lei, and S. Wang, Orbital-selective Dirac fermions and extremely flat bands in frustrated kagome-lattice metal CoSn, Nat. Commun. **11**, 4002 (2020).

[8] M. Kang, S. Fang, L. Ye, H. C. Po, J. Denlinger, C. Jozwiak, A. Bostwick, E. Rotenberg, E. Kaxiras, J. G. Checkelsky, and R. Comin, Topological flat bands in frustrated kagome lattice CoSn, Nat. Commun. **11**, 4004 (2020).

[9] S. Nakatsuji, N. Kiyohara, and T. Higo, Large anomalous Hall effect in a non-collinear antiferromagnet at room temperature, Nature (London) **527**, 212 (2015).

[10] A. K. Nayak, J. E. Fischer, Y. Sun, B. Yan, J. Karel, A. C. Komarek, C. Shekhar, N. Kumar, W. Schnelle, J. Kübler, C. Felser, and S. S. P. Parkin, Large anomalous Hall effect driven by a nonvanishing Berry curvature in the noncolinear antiferromagnet Mn_3Ge, Sci. Adv. **2**, e1501870 (2016).

[11] J.-X. Yin, B. Lian, and M. Z. Hasan, Topological kagome magnets and superconductors, Nature (London) **612**, 647 (2022).

[12] G. Venturini, B. C. E. Idrissi, and B. Malaman, Magnetic properties of RMn_6Sn_6 (R = Sc, Y, Gd-Tm, Lu) compounds with $HfFe_6Ge_6$ type structure, J. Magn. Magn. Mater. **94**, 35 (1991).

[13] W. Ma, X. Xu, J.-X. Yin, H. Yang, H. Zhou, Z.-J. Cheng, Y. Huang, Z. Qu, F. Wang, M. Z. Hasan, and S. Jia, Rare earth engineering in RMn_6Sn_6 ($R = Gd-Tm$, Lu) topological kagome magnets, Phys. Rev. Lett. **126**, 246602 (2021).

[14] Y. Feng and Q. Yang, Enabling triferroics coupling in breathing kagome lattice Nb_3X_8 (X = Cl, Br, I) monolayers, J. Mater. Chem. C **11**, 5762 (2023).

[15] B. R. Ortiz, L. C. Gomes, J. R. Morey, M. Winiarski, M. Bordelon, J. S. Mangum, I. W. H. Oswald, J. A. Rodriguez-Rivera, J. R. Neilson, S. D. Wilson, E. Ertekin, T. M. McQueen, and E. S. Toberer, New kagome prototype materials: Discovery of KV_3Sb_5, RbV_3Sb_5, and CsV_3Sb_5, Phys. Rev. Mater. **3**, 094407 (2019).

[16] C. Broyles, D. Graf, H. Yang, X. Dong, H. Gao, and S. Ran, Effect of the interlayer ordering on the Fermi surface of kagome superconductor CsV_3Sb_5 revealed by quantum oscillations, Phys. Rev. Lett. **129**, 157001 (2022).

[17] H. Tan, Y. Liu, Z. Wang, and B. Yan, Charge density waves and electronic properties of superconducting kagome metals, Phys. Rev. Lett. **127**, 046401 (2021).

[18] B. R. Ortiz, S. M. L. Teicher, Y. Hu, J. L. Zuo, P. M. Sarte, E. C. Schueller, A. M. Milinda Abeykoon, M. J. Krogstad, S. Rosenkranz, R. Osborn, R. Seshadri, L. Balents, J. He, and S. D. Wilson, Csv_3Sb_5: A $\mathbb{A}_2$ topological kagome metal with a superconducting ground state, Phys. Rev. Lett. **125**, 247002 (2020).

[19] H. Li, T. T. Zhang, T. Yilmaz, Y. Y. Pai, C. E. Marvinney, A. Said, Q. W. Yin, C. S. Gong, Z. J. Tu, E. Vescovo, C. S. Nelson, R. G. Moore, S. Murakami, H. C. Lei, H. N. Lee, B. J. Lawrie, and H. Miao, Observation of unconventional charge density wave without acoustic phonon anomaly in kagome superconductors AV_3Sb_5 (a = Rb, Cs), Phys. Rev. X **11**, 031050 (2021).

[20] K. Nakayama, Y. Li, T. Kato, M. Liu, Z. Wang, T. Takahashi, Y. Yao, and T. Sato, Multiple energy scales and anisotropic energy gap in the charge-density-wave phase of the kagome superconductor CsV_3Sb_5, Phys. Rev. B **104**, L161112 (2021).

[21] S. Cho, H. Ma, W. Xia, Y. Yang, Z. Liu, Z. Huang, Z. Jiang, X. Lu, J. Liu, Z. Liu, J. Li, J. Wang, Y. Liu, J. Jia, Y. Guo, J. Liu, and D. Shen, Emergence of new van Hove singularities in the charge density wave state of a topological kagome metal RbV_3Sb_5, Phys. Rev. Lett. **127**, 236401 (2021).

[22] J. Zhao, W. Wu, Y. Wang, and S. A. Yang, Electronic correlations in the normal state of the kagome superconductor KV_3Sb_5, Phys. Rev. B **103**, L241117 (2021).

[23] Z. Liang, X. Hou, F. Zhang, W. Ma, P. Wu, Z. Zhang, F. Yu, J.-J. Ying, K. Jiang, L. Shan, Z. Wang, and X.-H. Chen, Three-dimensional charge density wave and surface-dependent vortex-core states in a kagome superconductor CsV_3Sb_5, Phys. Rev. X **11**, 031026 (2021).

[24] Y. Wang, S. Yang, P. K. Sivakumar, B. R. Ortiz, S. M. L. Teicher, H. Wu, A. K. Srivastava, C. Garg, D. Liu, S. S. P. Parkin, E. S. Toberer, T. McQueen, S. D. Wilson, and M. N. Ali, Anisotropic proximity-induced superconductivity and edge supercurrent in kagome metal, $K_{1-x}V_3Sb_5$, arXiv:2012.05898.

[25] Z. Wang, S. Ma, Y. Zhang, H. Yang, Z. Zhao, Y. Ou, Y. Zhu, S. Ni, Z. Lu, H. Chen, K. Jiang, L. Yu, Y. Zhang, X. Dong, J. Hu, H.-J. Gao, and Z. Zhao, Distinctive momentum dependent charge-density-wave gap observed in CsV_3Sb_5 superconductor with topological kagome lattice, arXiv:2104.05556.

[26] T. Qian, M. H. Christensen, C. Hu, A. Saha, B. M. Andersen, R. M. Fernandes, T. Birol, and N. Ni, Revealing the competition between charge density wave and superconductivity in CsV_3Sb_5 through uniaxial strain, Phys. Rev. B **104**, 144506 (2021).

[27] F. H. Yu, D. H. Ma, W. Z. Zhuo, S. Q. Liu, X. K. Wen, B. Lei, J. J. Ying, and X. H. Chen, Unusual competition of superconductivity and charge-density-wave state in a compressed topological kagome metal, Nat. Commun. **12**, 3645 (2021).

[28] K. Y. Chen, N. N. Wang, Q. W. Yin, Y. H. Gu, K. Jiang, Z. J. Tu, C. S. Gong, Y. Uwatoko, J. P. Sun, H. C. Lei, J. P. Hu, and J.-G. Cheng, Double superconducting dome and triple enhancement of T_c in the kagome superconductor CsV_3Sb_5 under high pressure, Phys. Rev. Lett. **126**, 247001 (2021).

[29] Q. Wang, P. Kong, W. Shi, C. Pei, C. Wen, L. Gao, Y. Zhao, Q. Yin, Y. Wu, G. Li, H. Lei, J. Li, Y. Chen, S. Yan, and Y. Qi, Charge density wave orders and enhanced superconductivity under pressure in the kagome metal CsV_3Sb_5, Adv. Mater. **33**, 2102813 (2021).

[30] N. Shumiya, M. S. Hossain, J.-X. Yin, Y.-X. Jiang, B. R. Ortiz, H. Liu, Y. Shi, Q. Yin, H. Lei, S. S. Zhang, G. Chang, Q. Zhang, T. A. Cochran, D. Multer, M. Litskevich, Z.-J. Cheng, X. P. Yang, Z. Guguchia, S. D. Wilson, and M. Z. Hasan, Intrinsic

nature of chiral charge order in the kagome superconductor RbV$_3$Sb$_5$, Phys. Rev. B **104**, 035131 (2021).

[31] Z. Wang, Y.-X. Jiang, J.-X. Yin, Y. Li, G.-Y. Wang, H.-L. Huang, S. Shao, J. Liu, P. Zhu, N. Shumiya, M. S. Hossain, H. Liu, Y. Shi, J. Duan, X. Li, G. Chang, P. Dai, Z. Ye, G. Xu, Y. Wang, H. Zheng, J. Jia, M. Z. Hasan, and Y. Yao, Electronic nature of chiral charge order in the kagome superconductor CsV$_3$Sb$_5$, Phys. Rev. B **104**, 075148 (2021).

[32] F. H. Yu, T. Wu, Z. Y. Wang, B. Lei, W. Z. Zhuo, J. J. Ying, and X. H. Chen, Concurrence of anomalous Hall effect and charge density wave in a superconducting topological kagome metal, Phys. Rev. B **104**, L041103 (2021).

[33] H. Li, H. Zhao, B. R. Ortiz, Y. Oey, Z. Wang, S. D. Wilson, and I. Zeljkovic, Unidirectional coherent quasiparticles in the high-temperature rotational symmetry broken phase of AV$_3$Sb$_5$ kagome superconductors, Nat. Phys. **19**, 637 (2023).

[34] Y.-X. Jiang, J.-X. Yin, M. M. Denner, N. Shumiya, B. R. Ortiz, G. Xu, Z. Guguchia, J. He, M. S. Hossain, X. Liu, J. Ruff, L. Kautzsch, S. S. Zhang, G. Chang, I. Belopolski, Q. Zhang, T. A. Cochran, D. Multer, M. Litskevich, Z.-J. Cheng, X. P. Yang, Z. Wang, R. Thomale, T. Neupert, S. D. Wilson, and M. Z. Hasan, Unconventional chiral charge order in kagome superconductor KV$_3$Sb$_5$, Nat. Mater. **20**, 1353 (2021).

[35] B. Hu, Y. Ye, Z. Huang, X. Han, Z. Zhao, H. Yang, H. Chen, and H.-J. Gao, Robustness of the unidirectional stripe order in the kagome superconductor CsV$_3$Sb$_5$, Chin. Phys. B **31**, 058102 (2022).

[36] C. Xu, S. Wu, G.-X. Zhi, G. Cao, J. Dai, C. Cao, X. Wang, and H.-Q. Lin, Frustrated altermagnetism and charge density wave in kagome superconductor CsCr$_3$Sb$_5$, arXiv:2309.14812.

[37] Y. Liu, Z.-Y. Liu, J.-K. Bao, P.-T. Yang, L.-W. Ji, J.-Y. Liu, C.-C. Xu, W.-Z. Yang, W.-L. Chai, J.-Y. Lu, C.-C. Liu, B.-S. Wang, H. Jiang, Q. Tao, Z. Ren, X.-F. Xu, C. Cao, Z.-A. Xu, J.-G. Cheng, and G.-H. Cao, Superconductivity emerged from density-wave order in a kagome bad metal, arXiv:2309.13514.

[38] K. M. Shen and J. C. S. Davis, Cuprate high-tc superconductors, Mater. Today **11**, 14 (2008).

[39] H. Yang, Z. Zhao, X.-W. Yi, J. Liu, J.-Y. You, Y. Zhang, H. Guo, X. Lin, C. Shen, H. Chen, X. Dong, G. Su, and H.-J. Gao, Titanium-based kagome superconductor CsTi$_3$Bi$_5$ and topological states, arXiv:2209.03840.

[40] H. Yang, Y. Ye, Z. Zhao, J. Liu, X.-W. Yi, Y. Zhang, J. Shi, J.-Y. You, Z. Huang, B. Wang, J. Wang, H. Guo, X. Lin, C. Shen, W. Zhou, H. Chen, X. Dong, G. Su, Z. Wang, and H.-J. Gao, Superconductivity and orbital-selective nematic order in a new titanium based kagome metal CsTi$_3$Bi$_5$, arXiv:2211.12264.

[41] Y. Hu, C. Le, Y. Zhang, Z. Zhao, J. Liu, J. Ma, N. C. Plumb, M. Radovic, H. Chen, A. P. Schnyder, X. Wu, X. Dong, J. Hu, H. Yang, H.-J. Gao, and M. Shi, Non-trivial band topology and orbital-selective electronic nematicity in a titanium-based kagome superconductor, Nat. Phys. **19**, 1827 (2023).

[42] Y. Zhou, L. Chen, X. Ji, C. Liu, K. Liao, Z. Guo, J. Wang, H. Weng, and G. Wang, Physical properties, electronic structure, and strain-tuned monolayer of the weak topological insulator RbTi$_3$Bi$_5$ with kagome lattice, arXiv:2301.01633.

[43] Z. Jiang, Z. Liu, H. Ma, W. Xia, Z. Liu, J. Liu, S. Cho, Y. Yang, J. Ding, J. Liu, Z. Huang, Y. Qiao, J. Shen, W. Jing, X. Liu, J. Liu, Y. Guo, and D. Shen, Flat bands, non-trivial band topology and rotation symmetry breaking in layered kagome-lattice RbTi$_3$Bi$_5$, Nat. Commun. **14**, 4892 (2023).

[44] Y. Li, H. Tan, and B. Yan, Quantum oscillations with topological phases in a kagome metal CsTi$_3$Bi$_5$, arXiv:2307.04750.

[45] X. Dong, Y. Zhang, X. Yi, Z. Zhao, J. Liu, Z. Liu, A. Xu, D. Li, Z. Lu, S. Ma, Y. Liu, J. Lu, H. Zhang, H. Chen, S. Li, J. Cheng, G. Su, H. Yang, S. Du, and Z. Zhao, de Haas–van Alphen oscillation reveals nontrivial Fermi surface topology in kagome superconductor RbTi$_3$Bi$_5$ (2023).

[46] D. Werhahn, B. R. Ortiz, A. K. Hay, S. D. Wilson, R. Seshadri, and D. Johrendt, The kagomé metals RbTi$_3$Bi$_5$ and CsTi$_3$Bi$_5$, Z. Naturforsch. B **77**, 757 (2022).

[47] C. T. Van Degrift, Tunnel diode oscillator for 0.001 ppm measurements at low temperatures, Rev. Sci. Instrum. **46**, 599 (2008).

[48] T. Coffey, Z. Bayindir, J. F. DeCarolis, M. Bennett, G. Esper, and C. C. Agosta, Measuring radio frequency properties of materials in pulsed magnetic fields with a tunnel diode oscillator, Rev. Sci. Instrum. **71**, 4600 (2000).

[49] G. Kresse and J. Furthmüller, Efficient iterative schemes for *ab initio* total-energy calculations using a plane-wave basis set, Phys. Rev. B **54**, 11169 (1996).

[50] J. P. Perdew, K. Burke, and M. Ernzerhof, Generalized gradient approximation made simple, Phys. Rev. Lett. **77**, 3865 (1996).

[51] S. Grimme, J. Antony, S. Ehrlich, and H. Krieg, A consistent and accurate *ab initio* parametrization of density functional dispersion correction (DFT-D) for the 94 elements H-Pu, J. Chem. Phys. **132**, 154104 (2010).

[52] K. Koepernik and H. Eschrig, Full-potential nonorthogonal local-orbital minimum-basis band-structure scheme, Phys. Rev. B **59**, 1743 (1999).

[53] H. Tan, Y. Li, Y. Liu, D. Kaplan, Z. Wang, and B. Yan, Emergent topological quantum orbits in the charge density wave phase of kagome metal CsV$_3$Sb$_5$, npj Quantum Mater. **8**, 39 (2023).

[54] D. Shoenberg, Theory of the de Haas-van Alphen effect, J. Phys. F **18**, 49 (1988).

[55] D. Shoenberg, *Magnetic Oscillations in Metals*, Cambridge Monographs on Physics (Cambridge University Press, Cambridge, 2009).

[56] See Supplemental Material at http://link.aps.org/supplemental/10.1103/PhysRevMaterials.8.024003 for information regarding background subtractions, harmonic analysis, and analysis of the other data sets that were taken but not displayed in the main text.